Target kinematic state estimation with passive multistatic radar

Ma, Hui; Antoniou, Michail; Stove, Andrew; Cherniakov, Mike

Target Kinematic State Estimation with Passive Multistatic Radar

Hui Ma, Michail Antoniou, *Senior Member, IEEE*, Andrew G. Stove, *Senior Member, IEEE,* Mikhail Cherniakov

Abstract— **This paper examines methods for and results of determining the instantaneous kinematic state of a target, i.e. its velocity and heading, using passive multistatic radar. This is achieved by combining bistatic target range and Doppler information obtained by multiple bistatic transmitter-receiver pairs, to estimate the appropriate target velocity vector. This estimation is provided as a set of closed-form equations, derived for a general case applicable to an arbitrary number of transmitters. The feasibility of the proposed approach and its accuracy predictions, as a function of the number of transmitters, are experimentally confirmed via a dedicated experimental campaign with Global Navigation Satellite Systems (GNSS) as transmitters of opportunity, where two different and relatively slow-moving maritime targets were in the field of view of up to 12 satellite transmitters belonging to different satellite constellations (GPS, GLONASS and Galileo) simultaneously.**

Index Terms—**GNSS-based radar, multistatic radar, multiple constellations, target localization, velocity estimation.**

I. INTRODUCTION

Over the last decades, passive bistatic radar has reached a significant level of maturity [1], A multitude of potential illuminators of opportunity have been brought forward and investigated at the theoretical, experimental and sometimes even commercial level, such as FM [2], Digital Video Broadcasting-Terrestrial (DVB-T) [3][4], Digital Audio Broadcasting (DAB) [5], the Global System for Mobile Communication (GSM) [6][7], WiFi [8], WiMAX [9][10], and Global Navigation Satellite Systems (GNSS) [11][12], among others.

An essential purpose of these radar systems is surveillance, manifested by target detection and the estimation of bistatic target range and Doppler. A next natural, and important, step is the determination of a target's kinematic state, i.e. its location and, in general, velocity in the case of a moving target. However, a single range and Doppler measurement from a bistatic transmitter-receiver pair is not generally sufficient to extract this information. For this reason, multistatic, rather than bistatic, radar systems can be considered. In this configuration, it has been shown that a number of bistatic range and/or Doppler measurements, obtained from a number of spatially

separated transmitters and/or receivers, can be combined to estimate target location by multi-lateration [13]-[15] or multistatic target tracking techniques [16]-[19] for various types of radar systems, e.g. MIMO radar, network radar, multistatic passive radar, etc.

Mature theoretical models and algorithms have been developed for target localization, based on straightforward geometric physical models. The two mainstream methods of solving the multi-lateration problem are analyzed in [13] and are applied to the localization of stationary target. This method is extended to the moving target and verified with experimental results [20][21]. Having estimates of target instantaneous location, estimates of the target's instantaneous velocity vector are needed to create the description of its kinematic state, on which some other recent work has concentrated. The methods for evaluating the target velocity and its covariance matrix have been investigated based on the maximum likelihood estimation theories [22]-[24] or sparse Bayesian learning [25], etc. However, practical work and experimental results in this area are rarely seen for verifying the proposed algorithms and much less compared to work on target location [26]-[28], let alone with large numbers of transmitters and/or receivers. Moreover, in the previous works, either the multi-transmitter or multi-receiver networks have not been considered to be moving, but the complex influence to the Doppler by the transmitters' or receivers' motion cannot be neglected when it exists.

The aim of this paper is to derive a basis for estimating the instantaneous velocity vector of a target in a multistatic radar system, to predict its accuracy as a function of the number of transmitter-receiver pairs, and to confirm experimentally its feasibility and performance.

It is shown that the velocity vector can be extracted from multiple instantaneous bistatic Doppler measurements and from the instantaneous target location via the appropriate closed-form equations. In that case closed-form equations can also be derived to quantify the expected accuracy. It is noted here that theoretical analyses assume a passive multi-static radar system based on GNSS as illuminators of opportunity since experiments to confirm the proposed approach were conducted with such a system. However, the analysis is generic and therefore can be applied to any multistatic radar system, active or passive.

As noted in passing, an important aspect of the work reported here is that both aspects of the theoretical work, i.e. both the viability of the concept and its accuracy, have been confirmed

with experimental data in a real environment. In this experimental campaign, two different and relatively slow-moving maritime targets were detected by up to 12 GNSS satellites simultaneously, from all 3 major GNSS constellations. In addition, Automatic Identification System (AIS) data were available for providing the locations of both targets as the ground truth. During the velocity estimation process, the target locations were obtained following the spherical intersection method in [13] and used as one of the input parameters, with the AIS track as the reference and alternative.

The remaining content of this paper is arranged as follows: Section II derives the velocity vector estimation process and its accuracy. Next, in Section III, the experimental setup and the range-Doppler processing results of the practical multistatic GNSS-based radar for the confirmation of the concept are presented. Section IV presents the experimental results of the velocity vector estimation and compares them with the ground truth. Finally, a conclusion is given in Section V.

Notations: We list here some notational convention to be used throughout this paper. Math bold is used for vectors and matrices, to be separated from scalars.

A^T	Transpose of A
diag($\cdots$)	A diagonal matrix with given entries
E(A)	Expected value of A
$\partial A/\partial x$	The partial derivative of A with respect to x
$\circ$	Pointwise product operator
$\otimes$	Kronecker product operator

II. Target Velocity Vector Estimation Algorithm with Multistatic radar

A. Geometry and Problem Description

The system geometry in local coordinates is shown in Fig.1 and the total number of satellites that are used as transmitter of opportunity is represented by *N*. To analyze a passive radar with multiple satellites and one single receiver, we can, with no loss of generality, set the origin at the position of the receiver, so the location of the receiver is (0,0,0). Since the ranges are relatively short the ground or sea surface is modeled as a flat plane parallel to the (X,Y,0) plane. The coordinates of the target
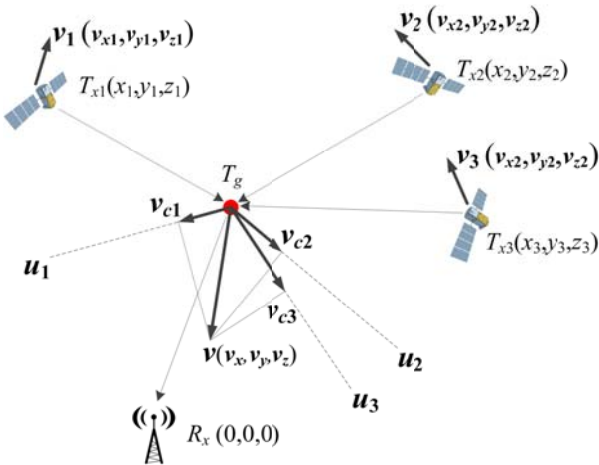

Fig. 1. Multistatic satellite-borne passive radar (number of satellites: *N*=3).

and its velocity are denoted as:

$$T_g = \mathbf{x} = (x, y, z)^T, \quad (1)$$

and

$$\mathbf{v} = (v_x, v_y, v_z)^T. \quad (2)$$

Similarly, the position and velocity of the *i*-th satellite are:

$$T_{xi} = \mathbf{x}_i = (x_i, y_i, z_i)^T, \quad (3)$$

and

$$\mathbf{v}_i = (v_{xi}, v_{yi}, v_{zi})^T. \quad (4)$$

with the subscript *i* for numbering the satellites. The vectors $\mathbf{v}_{ci}$ denotes the projection of $\mathbf{v}$ along the bisector of the corresponding satellite.

And we define the range between the *i*-th satellite and the target as:

$$T_i = \|\mathbf{x}_i - \mathbf{x}\| = \sqrt{(x_i-x)^2+(y_i-y)^2+(z_i-z)^2}, \quad (5)$$

and the range between the receiver and the target as:

$$R_0 = \|\mathbf{x}\| = \sqrt{x^2+y^2+z^2}. \quad (6)$$

Through a basic range-Doppler processing discussed in [20], the bistatic ranges and Doppler for particular target can be obtained using standard bistatic radar approaches. For further achieving the target localisation, we have discussed the algorithm, by applying multilateration (MLAT) based on the difference of bistatic distances.

The velocity vector estimation relies on the bistatic Doppler shifts. It is interesting to note that whereas a monostatic radar gives only one component of the velocity, the multiple different bistatic dimensions available in our bistatic scenario allow the complete target velocity vector to be obtained. Therefore, the velocity vector estimation essentially needs the particular bistatic geometries obtained, viz. the positions of transmitters, receiver and the target. Hence, except $\mathbf{v}$, other three parameters of the four mentioned above are already prior to known in our following analysis, while v is to be solved.

B. Bistatic Doppler

From its definition, the Doppler frequency is opposite in sign but equal in magnitude to the range rate divided by the wavelength. While for the bistatic case, the Doppler frequency due to the target is related to the target velocity's component along the bisector of bistatic angle.

In our case, and similar to many passive radars, one spare channel is used to receive the direct signal, propagating along the transmitter-to-receiver baseline. In the algorithm proposed in [20] by the authors for such a passive radar system, a pre-processing step of direct signal synchronization is considered to generate the reference based on the direct signal delay, phase and Doppler. This reference is used for range compression of the reflected signal from the target scene. Hence, at the output of the signal processing, for one particular target and particular satellite, we can detect the target 'relative' bistatic Doppler, which is the Doppler of the target reflection channel subtracted by that of the direct signal channel. The detected target Doppler of the i-th channel can be expressed as:

$$f_d = f_d^{\text{ref}} - f_d^{\text{dir}}, \quad (7)$$

with f_d^{ref} and f_d^{dir} being the Doppler shifts of the reflected and direct signals, respectively.

Considering the transmitter being on a Medium Earth Orbit (MEO), as GNSS are, and a stationary receiver, the motion of the transmitter contributes to the Doppler frequency too. Hence, taking T_{xi} in Fig.1 as an example, the Doppler frequencies on the reflected and direct signal channels can be written as:

$$f_{d\_i}^{\text{ref}} = \left(\boldsymbol{u}_i^T \boldsymbol{v} - \boldsymbol{h}_i^T \boldsymbol{v}_i \right) \big/ \lambda_i, \qquad (8)$$

$$f_{d\_i}^{\text{dir}} = -\boldsymbol{s}_i^T \boldsymbol{v}_i \big/ \lambda_i, \qquad (9)$$

where $\boldsymbol{u}_i$ is the vector along the bisector of the bistatic angle β_i formed with the i-th satellite. It is calculated by:

$$\boldsymbol{u}_i = \frac{\boldsymbol{x}_i - \boldsymbol{x}}{\|\boldsymbol{x}_i - \boldsymbol{x}\|} - \frac{\boldsymbol{x}}{\|\boldsymbol{x}\|}, \qquad (10)$$

and has a magnitude of $2\cos\left(\beta_i / 2 \right)$.

Similarly, $\boldsymbol{h}_i$ and $\boldsymbol{s}_i$ are respectively the unit vectors along the target-to-transmitter line and baseline:

$$\boldsymbol{h}_i = \frac{\boldsymbol{x}_i - \boldsymbol{x}}{\|\boldsymbol{x}_i - \boldsymbol{x}\|}, \qquad (11)$$

$$\boldsymbol{s}_i = \frac{\boldsymbol{x}_i}{\|\boldsymbol{x}_i\|}, \qquad (12)$$

and λ_i is the transmitted signal wavelength.

Defining the relative bistatic Doppler for the i-th satellite as f_{d_i}, then it can be calculated as:

$$f_{d\_i} = \left[\boldsymbol{u}_i^T \boldsymbol{v} - \left(\boldsymbol{h}_i^T - \boldsymbol{s}_i^T \right) \boldsymbol{v}_i \right] \big/ \lambda_i. \qquad (13)$$

C. Target Velocity Vector Estimation

While considering multiple satellites, (13) can be arranged into matrix form as:

$$\boldsymbol{U}\boldsymbol{v} = \boldsymbol{Z} + \boldsymbol{\Lambda}, \qquad (14)$$

with $\boldsymbol{U}$ being:

$$\boldsymbol{U} = \begin{bmatrix} \boldsymbol{u}_1^T \\ \boldsymbol{u}_2^T \\ \vdots \\ \boldsymbol{u}_N^T \end{bmatrix}_{N \times 3} = \begin{bmatrix} u_{x1} & u_{y1} & u_{z1} \\ u_{x2} & u_{y2} & u_{z2} \\ \vdots & \vdots & \vdots \\ u_{xN} & u_{yN} & u_{zN} \end{bmatrix}, \qquad (15)$$

and $\boldsymbol{Z}$ is a vector with each entry to be the relative bistatic speed corresponding to each satellite:

$$\boldsymbol{Z} = \begin{bmatrix} \left(\boldsymbol{h}_1^T - \boldsymbol{s}_1^T \right) \boldsymbol{v}_1 \\ \left(\boldsymbol{h}_2^T - \boldsymbol{s}_2^T \right) \boldsymbol{v}_2 \\ \vdots \\ \left(\boldsymbol{h}_N^T - \boldsymbol{s}_N^T \right) \boldsymbol{v}_N \end{bmatrix}_{N \times 1}, \qquad (16)$$

which is determined by the coordinate of the receiver and all satellites.

$\boldsymbol{\Lambda}$ is the vector of the products of carrier wavelengths detected bistatic Doppler frequencies for all satellites:

$$\boldsymbol{\Lambda} = \begin{bmatrix} \lambda_1 f_{d1} \\ \lambda_2 f_{d2} \\ \vdots \\ \lambda_N f_{dN} \end{bmatrix}_{N \times 1}. \qquad (17)$$

Therefore, we can solve the target velocity $\boldsymbol{v}$ as:

$$\boldsymbol{v} = \boldsymbol{\Upsilon} \left(\boldsymbol{Z} + \boldsymbol{\Lambda} \right), \qquad (18)$$

with

$$\boldsymbol{\Upsilon}_{3 \times N} = \left(\boldsymbol{U}^T \boldsymbol{U} \right)^{-1} \boldsymbol{U}^T. \qquad (19)$$

The existence of the solution of (18) is equivalent to the availability of $\boldsymbol{\Upsilon}_{3 \times N}$, i.e., depending on the characteristic of $\boldsymbol{U}$. While the rank of $\boldsymbol{U}$ is equal to three, the effective target velocity $\boldsymbol{v}$ can be obtained. It means that the effective spatial diversity should exist among at least three satellites for determining the three-dimensional target velocity.

D. Accuracy Analysis

The coefficient matrix $\boldsymbol{\Upsilon}$ is determined by the target location $\boldsymbol{x}$ and other prior conditions, while $\boldsymbol{\Lambda}$ is the measured parameter (the bistatic Doppler). To estimate the accuracy of the obtained velocity, we need to consider both the precision of target location $\boldsymbol{x}$ and the measuring precision of the bistatic Doppler f_{di}.

In the following analysis, the velocity error analysis is actually a process of error propagation. While applying to the practical data, the original error sources are obtained experimentally and the final error of the estimated parameter is then derived according to the relationship between the input and output parameters, that is, with regard to either target location or Doppler separately, a linear and well-defined process determined by the signal model, although there exists coupling between the two factors.

Denoting the covariance matrix of the target location and bistatic Doppler shifts as:

$$\boldsymbol{X}_{3 \times 3} = \mathrm{E}\left[\boldsymbol{x}\boldsymbol{x}^T \right] - \mathrm{E}\left[\boldsymbol{x} \right] \left(\mathrm{E}\left[\boldsymbol{x} \right] \right)^T. \qquad (20)$$

and

$$\boldsymbol{\Omega}_{N \times N} = \mathrm{E}\left[\boldsymbol{\Lambda}\boldsymbol{\Lambda}^T \right] - \mathrm{E}\left[\boldsymbol{\Lambda} \right] \left(\mathrm{E}\left[\boldsymbol{\Lambda} \right] \right)^T = \mathrm{diag}\left(\lambda_1^2 \sigma_{fd1}^2, \lambda_2^2 \sigma_{fd2}^2, \ldots, \lambda_N^2 \sigma_{fdN}^2 \right), \qquad (21)$$

with σ_{fdi}^2 representing the variance of the bistatic Doppler from the i-th satellite. Here the matrix $\boldsymbol{\Omega}_{N \times N}$ is diagonal, but it does not affect the generality of the following derivation.

To analyse the accuracy of the obtained target velocity, it is related with both $\boldsymbol{x}$ and $\boldsymbol{\Lambda}$, but independently. The covariance matrix of the target velocity is:

$$\begin{aligned} \boldsymbol{V}_{3 \times 3} &= \mathrm{cov}\left[\boldsymbol{\Upsilon}(\boldsymbol{Z}+\boldsymbol{\Lambda}), \boldsymbol{\Upsilon}(\boldsymbol{Z}+\boldsymbol{\Lambda}) \right] \\ &= \mathrm{E}\left[\boldsymbol{\Upsilon}(\boldsymbol{Z}+\boldsymbol{\Lambda})(\boldsymbol{Z}+\boldsymbol{\Lambda})^T \boldsymbol{\Upsilon}^T \right] - \mathrm{E}\left[\boldsymbol{\Upsilon}(\boldsymbol{Z}+\boldsymbol{\Lambda}) \right] \left(\mathrm{E}\left[\boldsymbol{\Upsilon}(\boldsymbol{Z}+\boldsymbol{\Lambda}) \right] \right)^T \end{aligned}, \qquad (22)$$

where $\boldsymbol{\Upsilon}$ and $\boldsymbol{Z}$ are related to the target location, viz. to the bistatic ranges (refer to the target localisation process in [13]) and $\boldsymbol{\Lambda}$ is related to the bistatic Doppler frequency.

Following the matrix multiplication rules, we can calculate the entry in the m-th row and n-th column of $\boldsymbol{V}_{3 \times 3}$ is:

$$V_{\mathrm{m,n}} = \sum_{i=1}^{N} \sum_{j=1}^{N} \left\{ \begin{aligned} &\mathrm{E}\left[\boldsymbol{\Upsilon}_{mi} \boldsymbol{\Upsilon}_{nj} (\boldsymbol{Z}_i + \boldsymbol{\Lambda}_i)(\boldsymbol{Z}_j + \boldsymbol{\Lambda}_j) \right] \\ &- \mathrm{E}\left[\boldsymbol{\Upsilon}_{mi} (\boldsymbol{Z}_i + \boldsymbol{\Lambda}_i) \right] \mathrm{E}\left[\boldsymbol{\Upsilon}_{nj} (\boldsymbol{Z}_j + \boldsymbol{\Lambda}_j) \right] \end{aligned} \right\}_{\mathrm{m,n}}, \qquad (23)$$

with every one or two subscript indices representing the corresponding entry in an array or a matrix. Since $\boldsymbol{\Upsilon}$ and $\boldsymbol{Z}$ are independent with $\boldsymbol{\Lambda}$, the expansion of (23) can be rearranged and then derived using a first-order Taylor series expansion as:

$$V_{\mathrm{m,n}} = \sum_{i=1}^{N}\sum_{j=1}^{N}\left\{\begin{array}{l} \mathrm{E}\left(\varUpsilon_{mi}\varUpsilon_{nj}Z_iZ_j\right)+\mathrm{E}\left(\varUpsilon_{mi}\varUpsilon_{nj}Z_i\right)\mathrm{E}\left(\varLambda_j\right) \\ +\mathrm{E}\left(\varUpsilon_{mi}\varUpsilon_{nj}Z_j\right)\mathrm{E}\left(\varLambda_i\right)+\mathrm{E}\left(\varUpsilon_{mi}\varUpsilon_{nj}\right)\mathrm{E}\left(\varLambda_i\varLambda_j\right) \\ -\mathrm{E}\left(\varUpsilon_{mi}Z_i\right)\mathrm{E}\left(\varUpsilon_{nj}Z_j\right)-\mathrm{E}\left(\varUpsilon_{mi}Z_i\right)\mathrm{E}\left(\varUpsilon_{nj}\right)\mathrm{E}\left(\varLambda_j\right) \\ -\mathrm{E}\left(\varUpsilon_{nj}Z_j\right)\mathrm{E}\left(\varUpsilon_{mi}\right)\mathrm{E}\left(\varLambda_i\right)-\mathrm{E}\left(\varUpsilon_{mi}\right)\mathrm{E}\left(\varUpsilon_{nj}\right)\mathrm{E}\left(\varLambda_i\varLambda_j\right) \end{array}\right\}$$

$$= \sum_{i=1}^{N}\sum_{j=1}^{N}\left\{\begin{array}{l} \mathrm{cov}\left(\varUpsilon_{mi}Z_i,\varUpsilon_{nj}Z_j\right) \\ +\mathrm{cov}\left(\varUpsilon_{mi}Z_i,\varUpsilon_{nj}\right)\mathrm{E}\left(\varLambda_j\right)+\mathrm{cov}\left(\varUpsilon_{mi},\varUpsilon_{nj}Z_j\right)\mathrm{E}\left(\varLambda_i\right) \\ +\mathrm{cov}\left(\varUpsilon_{mi},\varUpsilon_{nj}\right)\mathrm{E}\left(\varLambda_i\varLambda_j\right)+\mathrm{cov}\left(\varLambda_i,\varLambda_j\right)\mathrm{E}\left(\varUpsilon_{mi}\right)\mathrm{E}\left(\varUpsilon_{nj}\right) \end{array}\right\}$$

$$= \sum_{i=1}^{N}\sum_{j=1}^{N}\left\{\begin{array}{l} \dfrac{\partial(\varUpsilon_{mi}Z_i)}{\partial \boldsymbol{x}}\boldsymbol{X}\left[\dfrac{\partial(\varUpsilon_{nj}Z_j)}{\partial \boldsymbol{x}}\right]^{T}+\dfrac{\partial(\varUpsilon_{mi}Z_i)}{\partial \boldsymbol{x}}\boldsymbol{X}\left(\dfrac{\partial \varUpsilon_{nj}}{\partial \boldsymbol{x}}\right)^{T}\mathrm{E}\left(\varLambda_j\right) \\ +\dfrac{\partial \varUpsilon_{mi}}{\partial \boldsymbol{x}}\boldsymbol{X}\left[\dfrac{\partial(\varUpsilon_{nj}Z_j)}{\partial \boldsymbol{x}}\right]^{T}\mathrm{E}\left(\varLambda_i\right) \\ +\dfrac{\partial \varUpsilon_{mi}}{\partial \boldsymbol{x}}\boldsymbol{X}\left(\dfrac{\partial \varUpsilon_{nj}}{\partial \boldsymbol{x}}\right)^{T}\mathrm{E}\left(\varLambda_i\varLambda_j\right)+\boldsymbol{\varOmega}_{ij}\mathrm{E}\left(\varUpsilon_{mi}\right)\mathrm{E}\left(\varUpsilon_{nj}\right) \end{array}\right\},$$

$$(24)$$

where the Taylor analysis is made to all parameters of $\varUpsilon$, $\boldsymbol{Z}$ and $\varLambda$. Utilizing the algorithms of the partial differential formula and rearranging the terms, (24) can be written as:

$$V_{\mathrm{m,n}} = \sum_{i=1}^{N}\sum_{j=1}^{N}\left\{\begin{array}{l} \dfrac{\partial \varUpsilon_{mi}}{\partial \boldsymbol{x}}\boldsymbol{X}\left(\dfrac{\partial \varUpsilon_{nj}}{\partial \boldsymbol{x}}\right)^{T}\mathrm{E}\left(\boldsymbol{Z}_i+\varLambda_i\right)\mathrm{E}\left(\boldsymbol{Z}_j+\varLambda_j\right) \\ +\dfrac{\partial \boldsymbol{Z}_i}{\partial \boldsymbol{x}}\boldsymbol{X}\left(\dfrac{\partial \boldsymbol{Z}_j}{\partial \boldsymbol{x}}\right)^{T}\mathrm{E}\left(\varUpsilon_{mi}\right)\mathrm{E}\left(\varUpsilon_{nj}\right) \\ +\dfrac{\partial \boldsymbol{Z}_i}{\partial \boldsymbol{x}}\boldsymbol{X}\left(\dfrac{\partial \varUpsilon_{nj}}{\partial \boldsymbol{x}}\right)^{T}\mathrm{E}\left(\varUpsilon_{mi}\right)\mathrm{E}\left(\boldsymbol{Z}_j+\varLambda_j\right) \\ +\dfrac{\partial \varUpsilon_{mi}}{\partial \boldsymbol{x}}\boldsymbol{X}\left(\dfrac{\partial \boldsymbol{Z}_j}{\partial \boldsymbol{x}}\right)^{T}\mathrm{E}\left(\varUpsilon_{nj}\right)\mathrm{E}\left(\boldsymbol{Z}_i+\varLambda_i\right)+\boldsymbol{\varOmega}_{ij}\mathrm{E}\left(\varUpsilon_{mi}\varUpsilon_{nj}\right) \end{array}\right\}.$$

$$(25)$$

Defining a coefficient matrix as following:

$$\boldsymbol{C_o} = \begin{bmatrix} \boldsymbol{1}_{1\times N} & \boldsymbol{0}_{1\times N} & \boldsymbol{0}_{1\times N} \\ \boldsymbol{0}_{1\times N} & \boldsymbol{1}_{1\times N} & \boldsymbol{0}_{1\times N} \\ \boldsymbol{0}_{1\times N} & \boldsymbol{0}_{1\times N} & \boldsymbol{1}_{1\times N} \end{bmatrix},$$

$$(26)$$

with $\boldsymbol{I}_{3\times 3}$, $\boldsymbol{1}_{1\times N}$ and $\boldsymbol{0}_{1\times N}$ being matrices or arrays with all entries as 1 or 0 in the corresponding dimensions.

The summation symbols in (25) is equivalent to the matrix multiplication process as following:

$$V_{3\times 3} = \boldsymbol{C_o}\left\{\begin{array}{l} \left[\dfrac{\partial \varUpsilon_{3N\times 1}}{\partial \boldsymbol{x}}\boldsymbol{X}\left(\dfrac{\partial \varUpsilon_{3N\times 1}}{\partial \boldsymbol{x}}\right)^{T}\right]\circ\left\{\boldsymbol{I}_{3\times 3}\otimes\left[\mathrm{E}(\boldsymbol{D})\mathrm{E}(\boldsymbol{D}^{T})\right]\right\} \\ +\left[\left(\boldsymbol{I}_{3\times 1}\otimes\dfrac{\partial \boldsymbol{Z}}{\partial \boldsymbol{x}}\right)\boldsymbol{X}\left(\dfrac{\partial \varUpsilon_{3N\times 1}}{\partial \boldsymbol{x}}\right)^{T}\right]\circ\left\{\mathrm{E}\left(\varUpsilon_{3N\times 1}\right)\left[\boldsymbol{I}_{3\times 1}\otimes\mathrm{E}(\boldsymbol{D})\right]^{T}\right\} \\ +\left[\left(\dfrac{\partial \varUpsilon_{3N\times 1}}{\partial \boldsymbol{x}}\right)\boldsymbol{X}\left(\boldsymbol{I}_{3\times 1}\otimes\dfrac{\partial \boldsymbol{Z}}{\partial \boldsymbol{x}}\right)^{T}\right]\circ\left\{\left[\boldsymbol{I}_{3\times 1}\otimes\mathrm{E}(\boldsymbol{D})\right]\mathrm{E}\left(\varUpsilon_{3N\times 1}^{T}\right)\right\} \\ +\mathrm{E}\left(\varUpsilon_{3N\times 1}\varUpsilon_{3N\times 1}^{T}\right)\circ\boldsymbol{I}_{3\times 3}\otimes\boldsymbol{\varOmega} \\ +\mathrm{E}\left(\varUpsilon_{3N\times 1}\right)\mathrm{E}\left(\varUpsilon_{3N\times 1}^{T}\right)\circ\left[\boldsymbol{I}_{3\times 3}\otimes\left(\dfrac{\partial \boldsymbol{Z}}{\partial \boldsymbol{x}}\boldsymbol{X}\left(\dfrac{\partial \boldsymbol{Z}}{\partial \boldsymbol{x}}\right)^{T}\right)\right] \end{array}\right\}\boldsymbol{C_o^{T}}.$$

$$(27)$$

with $\varUpsilon_{3N\times 1}$ being a 3N-by-1 array, rearranged from 3-by-N matrix $\varUpsilon$ and sorted by rows. $(\partial\varUpsilon_{3N\times 1}/\partial\boldsymbol{x})_{3N\times 3}$ and $(\partial\boldsymbol{Z}/\partial\boldsymbol{x})_{N\times 3}$ are Jacobian matrices, and $\boldsymbol{D}=\boldsymbol{Z}+\varLambda$.

According to (19), $(\partial\varUpsilon/\partial\boldsymbol{x})$ can be calculated as:

$$\partial\varUpsilon/\partial\boldsymbol{x} = \left(\boldsymbol{U}^{T}\boldsymbol{U}\right)^{-1}\left(\partial\boldsymbol{U}/\partial\boldsymbol{x}\right)^{T}\left[\boldsymbol{I}-\boldsymbol{U}\left(\boldsymbol{U}^{T}\boldsymbol{U}\right)^{-1}\boldsymbol{U}^{T}\right]$$

$$-\left(\boldsymbol{U}^{T}\boldsymbol{U}\right)^{-1}\boldsymbol{U}^{T}\left(\partial\boldsymbol{U}/\partial\boldsymbol{x}\right)\left(\boldsymbol{U}^{T}\boldsymbol{U}\right)^{-1}\boldsymbol{U}^{T}$$

$$(28)$$

where $(\partial\boldsymbol{U}/\partial\boldsymbol{x})_{N\times 3}$ is the Jacobian matrix with all entries as 3×1 arrays and maintain this format during the matrix multiplication operation in (28). $(\partial\boldsymbol{U}/\partial\boldsymbol{x})$ can be calculated as:

$$\partial\boldsymbol{U}/\partial\boldsymbol{x} = \begin{bmatrix} \partial u_{x1}/\partial\boldsymbol{x} & \partial u_{y1}/\partial\boldsymbol{x} & \partial u_{z1}/\partial\boldsymbol{x} \\ \partial u_{x2}/\partial\boldsymbol{x} & \partial u_{y2}/\partial\boldsymbol{x} & \partial u_{z2}/\partial\boldsymbol{x} \\ \vdots & \vdots & \vdots \\ \partial u_{xN}/\partial\boldsymbol{x} & \partial u_{yN}/\partial\boldsymbol{x} & \partial u_{zN}/\partial\boldsymbol{x} \end{bmatrix}, \quad (29)$$

and based on (10), we can derive:

$$\partial u_{xi}/\partial\boldsymbol{x} = \begin{bmatrix} \dfrac{(x_i-x)^2}{T_i^3}+\dfrac{x^2}{R_0^3}-\dfrac{1}{T_i}-\dfrac{1}{R_0} \\ \dfrac{(x_i-x)(y_i-y)}{T_i^3}+\dfrac{xy}{R_0^3} \\ \dfrac{(x_i-x)(z_i-z)}{T_i^3}+\dfrac{xz}{R_0^3} \end{bmatrix}, \quad (30)$$

$$\partial u_{yi}/\partial\boldsymbol{x} = \begin{bmatrix} \dfrac{(x_i-x)(y_i-y)}{T_i^3}+\dfrac{xy}{R_0^3} \\ \dfrac{(y_i-y)^2}{T_i^3}+\dfrac{y^2}{R_0^3}-\dfrac{1}{T_i}-\dfrac{1}{R_0} \\ \dfrac{(y_i-y)(z_i-z)}{T_i^3}+\dfrac{yz}{R_0^3} \end{bmatrix}, \quad (31)$$

$$\partial u_{zi}/\partial\boldsymbol{x} = \begin{bmatrix} \dfrac{(x_i-x)(z_i-z)}{T_i^3}+\dfrac{xz}{R_0^3} \\ \dfrac{(y_i-y)(z_i-z)}{T_i^3}+\dfrac{yz}{R_0^3} \\ \dfrac{(z_i-z)^2}{T_i^3}+\dfrac{z^2}{R_0^3}-\dfrac{1}{T_i}-\dfrac{1}{R_0} \end{bmatrix}, \quad (32)$$

Therefore, $(\partial\varUpsilon/\partial\boldsymbol{x})$ can be obtained as an $N\times 3\times 3$ matrix and by rearranging the entries, we can get $(\partial\varUpsilon_{3N\times 1}/\partial\boldsymbol{x})$.

Similarly, $(\partial\boldsymbol{Z}/\partial\boldsymbol{x})$ can be calculated as:

$$(\partial\boldsymbol{Z}/\partial\boldsymbol{x}) = \begin{bmatrix} \dfrac{\partial\left(\boldsymbol{h}_1^{T}\boldsymbol{v}_1\right)}{\partial\boldsymbol{x}} \\ \dfrac{\partial\left(\boldsymbol{h}_2^{T}\boldsymbol{v}_2\right)}{\partial\boldsymbol{x}} \\ \vdots \\ \dfrac{\partial\left(\boldsymbol{h}_N^{T}\boldsymbol{v}_N\right)}{\partial\boldsymbol{x}} \end{bmatrix} = \begin{bmatrix} \dfrac{\left(\boldsymbol{h}_1^{T}\boldsymbol{v}_1\right)\boldsymbol{h}_1^{T}-\boldsymbol{v}_1^{T}}{\|\boldsymbol{x}_1-\boldsymbol{x}\|} \\ \dfrac{\left(\boldsymbol{h}_2^{T}\boldsymbol{v}_2\right)\boldsymbol{h}_2^{T}-\boldsymbol{v}_2^{T}}{\|\boldsymbol{x}_2-\boldsymbol{x}\|} \\ \vdots \\ \dfrac{\left(\boldsymbol{h}_N^{T}\boldsymbol{v}_N\right)\boldsymbol{h}_N^{T}-\boldsymbol{v}_N^{T}}{\|\boldsymbol{x}_N-\boldsymbol{x}\|} \end{bmatrix}. \quad (33)$$

By substituting (26-33) into (27), the covariance matrix $V_{3\times 3}$ can be calculated by $\boldsymbol{X}_{3\times 3}$ and $\boldsymbol{\varOmega}_{3\times 3}$.

It should be noted here that the variance of the target location is calculated considering only the first order of the Taylor expansion, that is, the linear component. The higher order components introduce more errors, but the approximate tendency can be indicated, as well as the order of magnitude.

III. EXPERIMENTAL MARITIME TARGET DETECTION

A. Experimental Setup, Scene and Parameters

To capture maritime target data, a passive receiver was located to the East of Portsmouth harbor, UK. The distributed bandwidths of the receiver covered the GPS L1 band, the GLONASS G1 band, and the Galileo E5a and E5b bands, all of
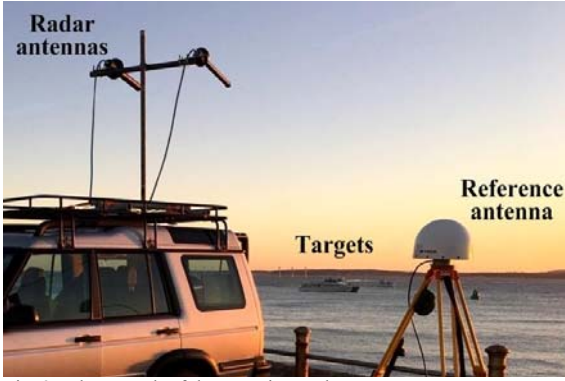
Fig. 2. Photograph of the experimental set up.

Fig. 3. Ferry tracks during the experiment (from GoogleEarth).

Fig. 4. Photograph of the ferry: Target A – St Cecilia

Fig. 5. Photograph of the ferry: Target B - Bretagne.

TABLE I   EXPERIMENTAL AND SIGNAL PROCESSING PARAMETERS

Parameter		Value	
		Target A	Target B
Sat 1	Constellation and number	Galileo – GSAT0206 (PRN30)	
	Bistatic angle	69.9° ~ 63.8°	79.1° ~ 56.5°
	Azimuth (relative to North)	63.8° ~ 63.1°	62.0° ~ 61.4°
	Elevation (relative to radar)	55.2° ~ 54.7°	54.0° ~ 53.5°
Sat 2	Constellation and number	Galileo – GSAT0211 (PRN02)	
	Bistatic angle	30.1° ~18.6 °	50.0° ~ 5.5°
	Azimuth (relative to North)	40.27° ~ 40.33°	40.45° ~ 40.53°
	Elevation (relative to radar)	7.3° ~ 6.7°	5.9° ~ 5.4°
Sat 3	Constellation and number	Glonass – COSMOS2457	
	Carrier frequency	1599.75 MHz	
	Bistatic angle	78.0° ~ 82.7 °	74.6° ~ 89.3°
	Azimuth (relative to North)	314.2° ~ 313.6°	312.4° ~ 311.6°
	Elevation (relative to radar)	67.8° ~ 68.8°	70.2° ~ 71.1°
Sat 4	Constellation and number	Glonass – COSMOS2425	
	Carrier frequency	1602.00 MHz	
	Bistatic angle	59.5° ~54.9 °	66.7° ~ 50.2°
	Azimuth (relative to North)	42.4° ~ 42.1°	41.6° ~ 41.4°
	Elevation (relative to radar)	53.5° ~ 52.5°	51.1° ~ 50.2°
Sat 5	Constellation and number	Glonass – COSMOS2477	
	Carrier frequency	1604.8125 MHz	
	Bistatic angle	54.7° ~ 66.0°	36.6° ~ 81.4°
	Azimuth (relative to North)	317.9° ~ 318.1°	318.4° ~ 318.6°
	Elevation (relative to radar)	16.1° ~ 16.9°	18.2° ~ 18.9°
Sat 6	Constellation and number	Glonass – COSMOS2459	
	Carrier frequency	1600.3125 MHz	
	Bistatic angle	65.7° ~78.3 °	47.1° ~ 96.4°
	Azimuth (relative to North)	305.4° ~ 304.7°	303.7° ~ 303.1°
	Elevation (relative to radar)	5.1° ~ 4.5°	3.7° ~ 3.2°
Sat 7	Constellation and number	GPS – BIIR02 (PRN13)	
	Bistatic angle	85.2° ~ 89.6°	78.2° ~ 94.7°
	Azimuth (relative to North)	293.2° ~ 293.9°	295.1° ~ 295.8°
	Elevation (relative to radar)	66.8° ~ 67.6°	68.8° ~ 69.6°
Sat 8	Constellation and number	GPS – BIIR04 (PRN20)	
	Bistatic angle	84.5° ~ 93.4°	72.9° ~ 105.9°
	Azimuth (relative to North)	289.0° ~ 288.0°	286.4° ~ 285.5°
	Elevation (relative to radar)	46.4° ~ 46.8°	47.4° ~ 47.8°
Sat 9	Constellation and number	GPS – BIIR05 (PRN28)	
	Bistatic angle	102.1° ~ 92.9°	113.6° ~ 79.8°
	Azimuth (relative to North)	118.0° ~ 117.1°	115.6° ~ 114.7°
	Elevation (relative to radar)	44.2° ~ 44.8°	45.6° ~ 46.0°
Sat 10	Constellation and number	GPS – BIIF05 (PRN30)	
	Bistatic angle	68.4° ~ 61.9°	79.0° ~53.8 °
	Azimuth (relative to North)	63.7° ~ 63.5°	63.2° ~ 63.1°
	Elevation (relative to radar)	52.6° ~ 51.8°	50.6° ~ 49.9°
Sat 11	Constellation and number	GPS – BIIRM04 (PRN15)	
	Bistatic angle	84.2° ~ 93.7°	68.1° ~ 106.0°
	Azimuth (relative to North)	288.1° ~ 288.3°	288.7° ~ 289.0°
	Elevation (relative to radar)	35.4° ~ 36.2°	37.3° ~ 38.0°
Sat 12	Constellation and number	GPS – BIIRM06 (PRN07)	
	Bistatic angle	50.2° ~ 39.5°	69.0° ~ 25.6°
	Azimuth (relative to North)	58.1° ~ 58.3°	58.6° ~ 58.8°
	Elevation (relative to radar)	19.6° ~ 18.9°	17.9° ~ 17.2°
GPS L1 band carrier frequency		1575.00 MHz	
Galileo E5 carrier frequency		1176.45 MHz (E5a) 1207.24 MHz (E5b)	
GPS C/A code bandwidth		1.023 MHz	
Glonass P code bandwidth		5.11 MHz	
Galileo E5 single channel bandwidth		10.23 MHz	
Sampling frequency		20 MHz	
Pulse repetition interval		1 millisecond	
Coherent processing interval		2.5 second	
Non-coherent processing interval		10 second	

which have been well-established in GNSS-based radar practice. All four bands were sampled at 20 MHz rate. Fig.2 shows a photograph of the experimental setup taken during the measurement.

The passive radar receiver is equipped with two channels. The reference channel is connected to a low gain antenna to receive the direct signal from all satellites in its field of view. The other channel, the signal channel is used for the target echo collection. In our experiments two high gain antennas were employed by the signal channel, with the center frequency at 1.2 GHz and 1.6 GHz respectively. Their signals were combined and filtered into four separate channels as the raw data for processing in a single wideband channel.

The moving targets of opportunity are commercial ferries running on a regular schedule so their departure and arrival times at the harbor were known. AIS transmitters are also installed on the ferries and continuously transmit their positions in real time. This information can be easily recorded by an AIS receiver and serves as the ground truth. Hence, the experimental target localization results can be verified with the AIS reference.

For undertaking off-line signal processing, we selected data from two different ferries chosen for their different dimensions and different kinematics. Fig.3 shows the ferry tracks and the position of the receiver. The figure also indicates the names of the ferries and the times when they passed through the field of view of the radar. The distance traveled by the 'Bretagne' ferry within the field of view is approximately 500 m, which indicates the scale of the map. The name of the first ferry is 'St Cecilia' (Target A). Its dimensions are 77.0 m in length and 17.2 m in beam and it is shown in Fig.4. The second ferry is 'Bretagne' (Target B), shown in Fig.5 with dimensions of 152.8 m × 26 m.

Throughout the recording periods each ferry was continuously illuminated by eleven or twelve satellites. Information of the satellites are given in Table I, including two Galileo satellites, four Glonass satellites and six GPS satellites. The reflected signal of Sat 9 (GPS – BIIR05) is seen only for 'St Cecilia' but except for that, both 'Bretagne' and 'St Cecilia' are detected by the receiver using all remaining 11 satellites.

B. Range-Doppler Processing Results

The Equivalent Isotopic Radiated Power (EIRP) of GNSS is relatively low. The radiated power is received by the target and then scattered according to its specific bistatic Radar Cross Section (RCS) pattern. The power finally reaching the passive receiver is generally only a very small part of the total power scattered by the targets. Taking into account the free space attenuation, which depends on the target range, the received target echo can be much lower than the receiver noise at the front end, even for the relatively large RCS target we have concerned. Coherent integration (matched filtering) is needed to suppress the noise and make the target signal stand out.

Based on that, the experimental dataset is treated by a range-Dopper (RD) processing, following the algorithm described in [20]. The algorithm is composed of two steps, first is range compression with matched filtering, and second is the

Fourier Transform along the Doppler dimension, with a pulse repetition interval (PRI) of 1 ms, conforming to the code length of all signals. This CPI can cover a Doppler detection range of 1 KHz, corresponding to the target speed around 200 knots, which is abundant for the aforementioned experimental scene and ensures that the detection of moving ships will not be compromised [29].

After range compression, the Signal-to-Noise Ratio (SNR) has been improved by the time-bandwidth product of the signal (typically 40 dB), but further integration of multiples of the 1 ms period is still both necessary and possible. This is achieved through a Fourier transform over the 'slow-time,' after the range compression. The main object of the RD processing is to extract the two-dimensional information from the collected echo, then it is capable to positioning the target in bistatic range and Doppler. Noted that since the satellites yield different bistatic ranges and Doppler frequencies, the RD processing needs to be applied to each individual satellite independently.

1) Coherent and Non-Coherent Integration

In order to perform the processing, the only parameter to be defined is the Coherent Processing Interval (CPI) for the FT. This determines the SNR gain and the Doppler resolution. As the CPI increases from the value of one PRI, the SNR improves linearly because of a strong coherence between adjacent slow-time samples of the same range bin. There are however three limits to the extent to which the integration time can be increased.

   i. The time for which the target remains visible, i.e. in the antenna beam of the receiver.

   ii. The rate at which the radar is required to deliver information to whoever or whatever is to make use of this information.

   iii. The kinematics of the target – its motion causes the signal to move from one range cell to the next, and its acceleration will cause it to move from one Doppler bin to another – and effect which also gets more significant because the Doppler bins become narrower as the integration time increases.

To achieve longer integration times, additional range alignment and phase compensation for changes in the Doppler shift are needed during signal processing [30].

An appropriate CPI was found to be 2.5 s, determined through the simple process of progressively increasing the coherent integration time and observing the SNR gain, to find the critical point when it starts to deviate from the coherent integration standard line [20].

In addition to performing coherent integration, four sets of adjacent RD maps are non-coherently combined afterwards, which reduces the fluctuations in the background noise level, resulting in the total data acquisition time of 10 s [20].

2) Range Doppler Histories

The RD histories for two targets are shown in Fig.6 and Fig.7, composed of results obtained from 12 or 11 satellites respectively. For example, Fig.6 shows the synchronous detections of Target A echo, respectively, obtained with single Galileo, Glonass and GPS satellites, and at the same time period.

In the figures, the RD data is mapped along two dimensions with the data magnitude given in dB. Here, 0 dB represent the point with highest intensity in the RD map. In every image, the noise floor has been aligned to -20 dB as the lower limit of the dynamic range. Each pixel takes 15 meters and 0.4 Hertz in range and Doppler respectively. Comparing the results, the most intuitive difference between the plots is in the range resolution, seen in the target and clutter responses, which varies with the different bandwidths of the different illuminating signals. We also observe different bistatic ranges and Doppler
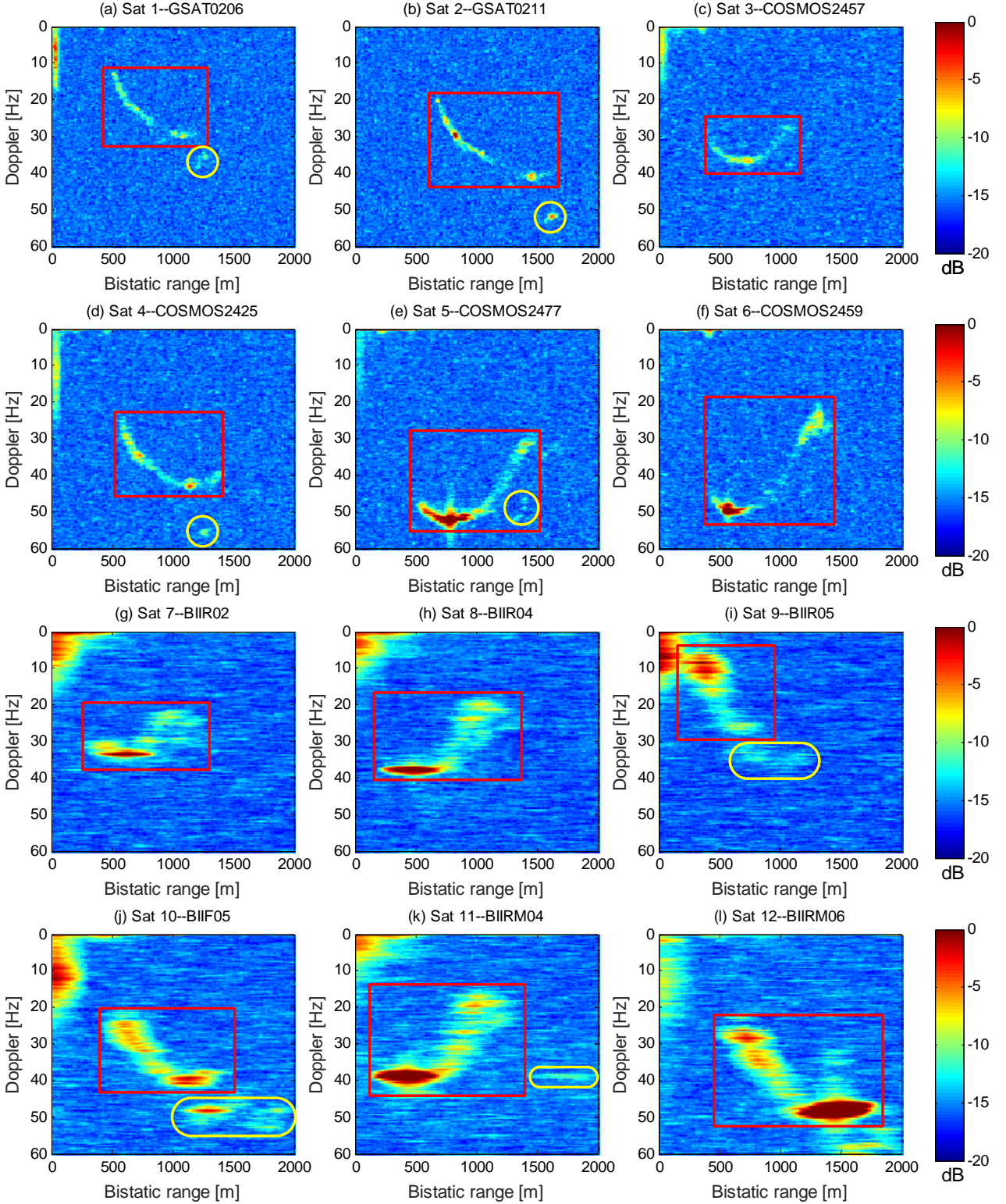
Fig. 6. RD histories of Target A by different satellites during the observation time. The procedure to obtain the RD history has been provided in [20] by the authors. The detected track of the ferry is outlined by the red rectangular box, and because the voyage of target A has some intersections with another target, detected by the radar as well, that detected results of that target are outlined by yellow circles or ellipses for avoiding any confusion.

frequency histories, and it is these different values that provide the starting point for the target velocity vector estimation concept.

IV. Experimental Target Velocity Vector Estimation

A. Bistatic Doppler Extraction

As mentioned above, the bistatic Doppler is deduced from each of the RD maps (as illustrated in Fig.6) by taking the peak of the target response which is extended due to the target size
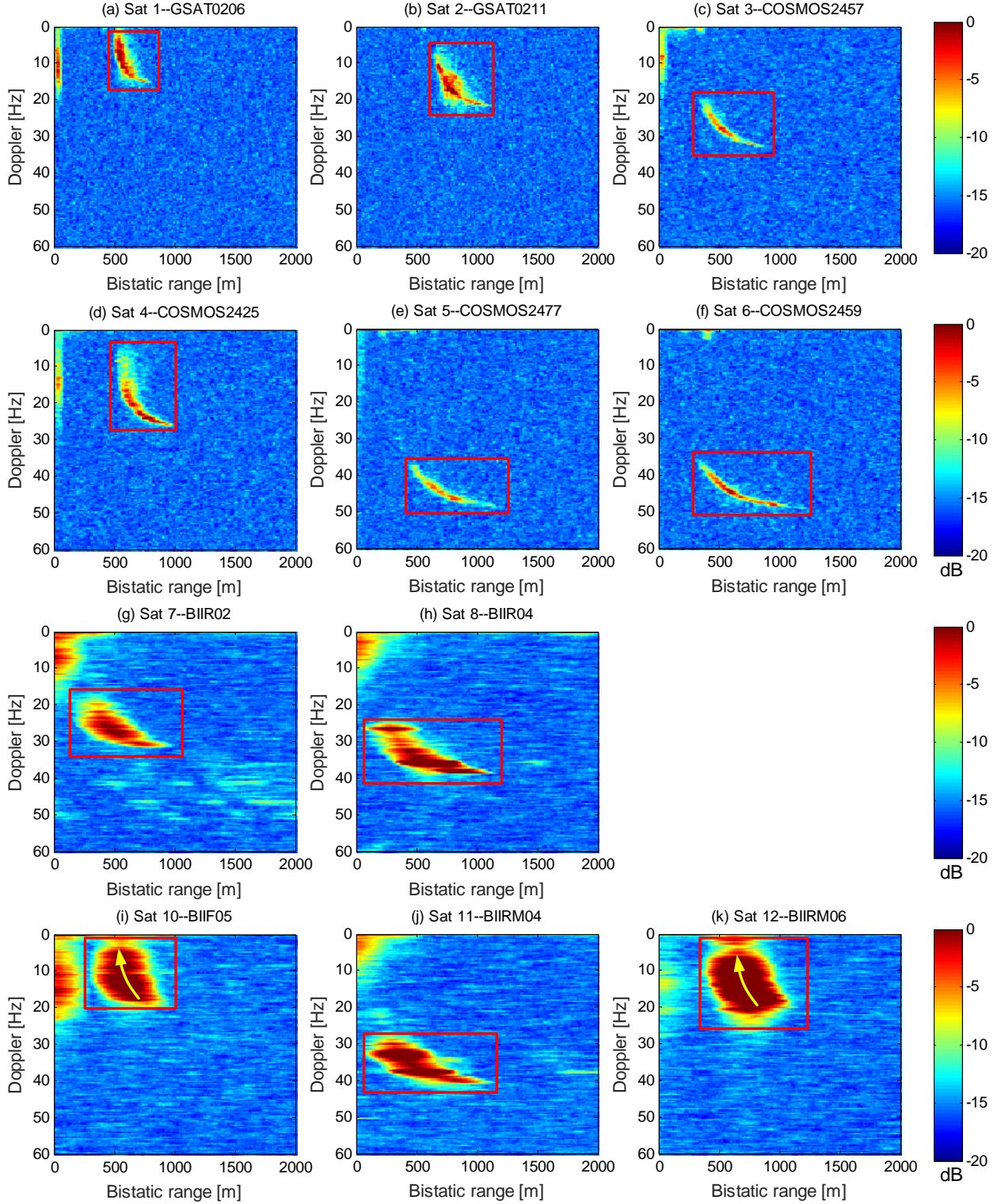
Fig. 7. RD histories of Target A by different satellites during the observation time. The procedure to obtain the RD history has been provided in [20] by the authors. The detected track of the ferry is outlined by the red rectangular box. Because the resolution cell of GPS signals diffuses in the range dimension, in figure (i) and (k), the target's moving tendency has been indicated by the yellow arrow.

and the Point Spread Function of the passive radar. As was done with the bistatic range estimates, we similarly obtain the bistatic Doppler frequencies with the different satellites. The experimental results are shown in Fig.8-9 for the two targets We have used the same colors and marker shapes to indicate the same satellite in all of the figures. Multiple Doppler results are plotted on the same figure to save space and are separated vertically for clarity, so the actual Doppler shifts are not shown, only the comparisons with the reference values. The mean values of the Doppler frequency for each satellite can, however, be found in the figure legend. A scale bar of 10 Hz is given for estimating the Doppler dynamic range for each individual satellite.

The r.m.s. accuracy of the data is about 0.4Hz. For a point target with a signal to noise ratio high enough to ensure detection, the accuracy will be dominated by the quantization error in the Doppler estimation process. For the certain coherent processing interval (CPI), the theoretical accuracy will be simply calculated by [CPI/sqrt(SNR)]. It can be seen that the accuracy is limited by the extended nature of the target, which allows the effective reflection point to wander across the length

and width of the ship. There is also a suggestion of bias errors in the data.

B. Doppler Reference Data

The reference bistatic Doppler is calculated from the AIS ground truth. The raw AIS data has very poor accuracy, since it is derived by differentiating the position data. It also contains some unreasonable changes between adjacent time points because the rate at which the AIS data is updated depends on its speed and when the ship moving slowly, it is considered unnecessary for the AIS system to report a new position with any significant frequency. In such a case, the AIS update period can be as long as more than 10 s. The errors caused by the limitations of the AIS data mean that the track derived from it is noisy and contains jumps. The reference data has therefore been smoothed by applying a Least Mean Square (LMS) estimate to the calculated Doppler and this smoothed value is used as the reference curve in Fig.8-9. Although this smoothed reference cannot represent the effects of acceleration very accurately, we can still use the curves to show the trend at least as a sanity check.
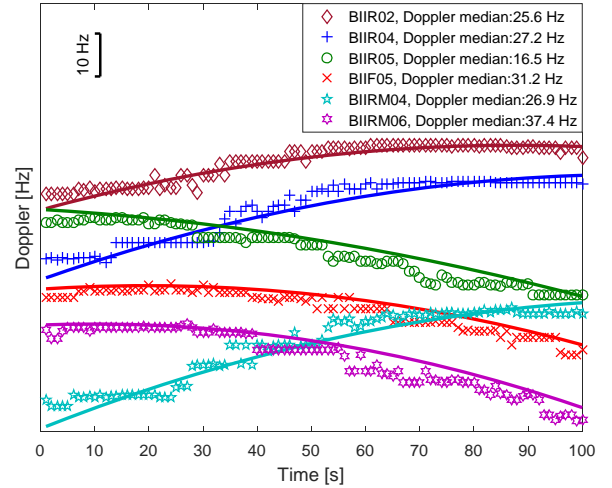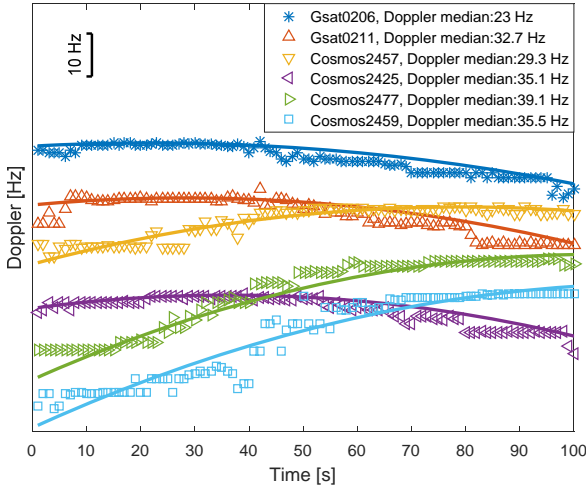

Fig. 8. Bistatic Doppler frequencies detected for Target A. The solid curves are the corresponding Doppler references obtained by the method in Section IV.B. Each curve corresponds to one certain satellite and arranged in the same color and the same coordinate frame with the detected Doppler of the same satellite.
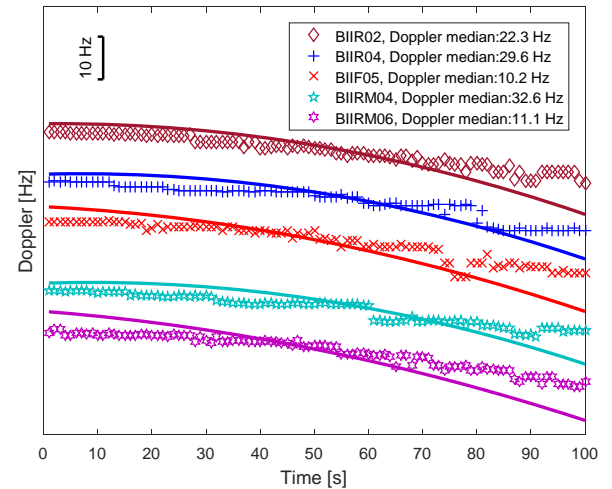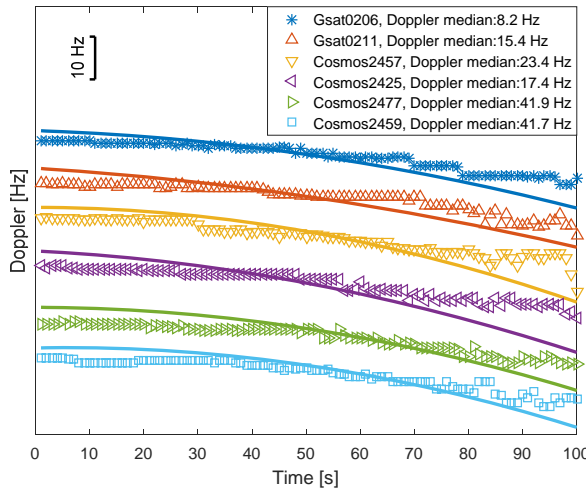

Fig. 9. Bistatic Doppler frequencies detected for Target B. The solid curves are the corresponding Doppler references obtained by the method in Section IV.B. Each curve corresponds to one certain satellite and arranged in the same color and the same coordinate frame with the detected Doppler of the same satellite.

C. *Target Velocity Estimation Results*

As discussed in section III, and analogously to what was done with the position data [20], we can use the measured Doppler frequencies, to estimate the velocity vectors of the targets. The velocity vector estimation results for Target A, are shown in Fig.10, 12 and 14, respectively illustrating the magnitude and azimuth of the horizontal velocities, and the vertical components of the velocity. Similar results for Target B are given in Fig.11, 13 and 15.

Taking Fig.10 as an example, the velocity estimation is processed using Doppler information of different numbers of

satellites. The number of satellites is counted starting from Sat1 and following the order in Table I. As discussed in section II, the target location is needed as an input parameter for the velocity estimation and affects the results. In our case, the target location can be obtained either through a multilateration target localization processing or directly by AIS. While the multilateration involved as the pre-processing, the bistatic ranges extracted from the same set of satellites as the bistatic Doppler frequencies are utilized, and then the obtained target location together with the bistatic Doppler frequencies are processed as in Section II.C. The estimated velocities by
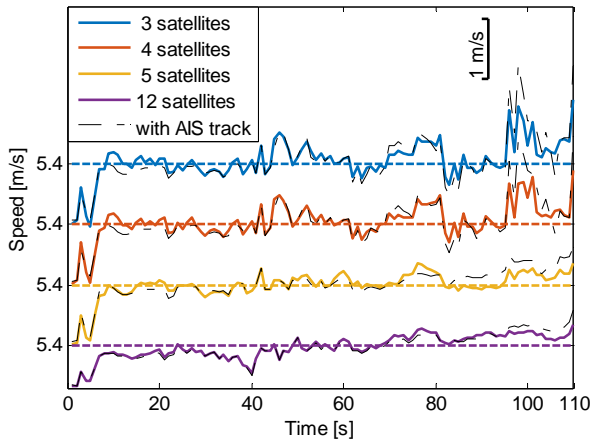

Fig. 10. Detected horizontal velocities of Target A.
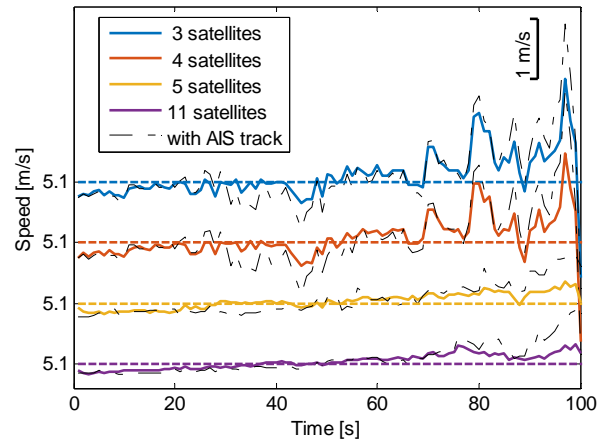

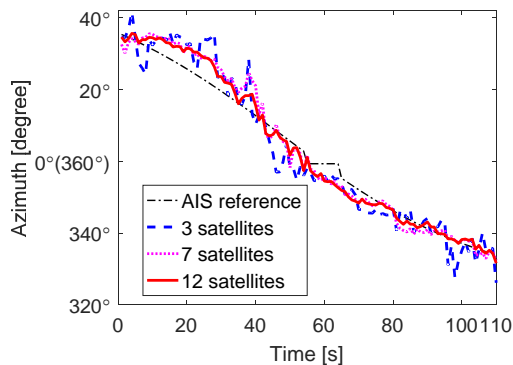Fig. 11. Detected horizontal velocities of Target B.

Fig. 12. The detected velocity azimuth on the sea level of Target A.
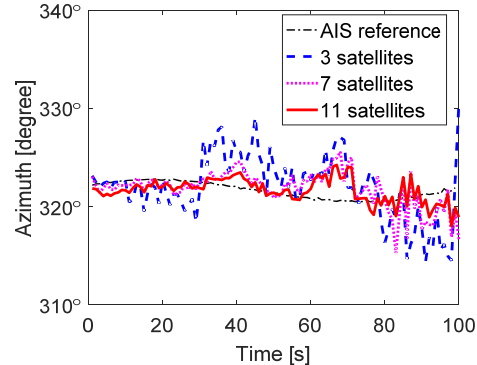

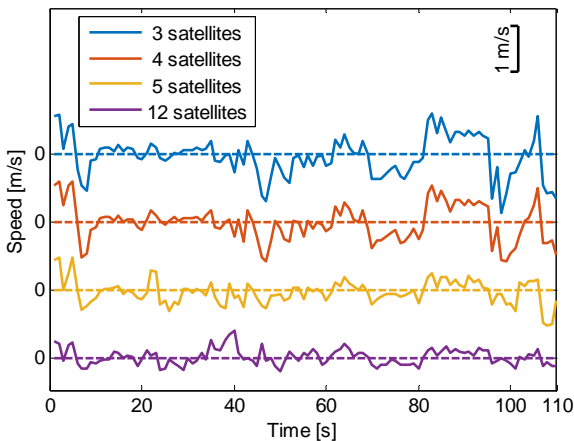Fig. 13. The detected velocity azimuth on the sea level of Target B.

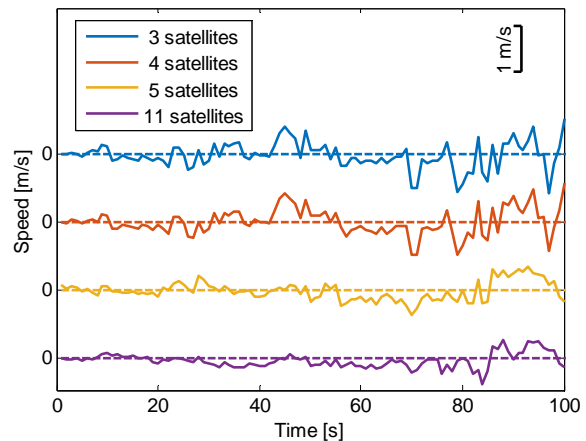Fig. 14. The vertical velocity component of Target A.

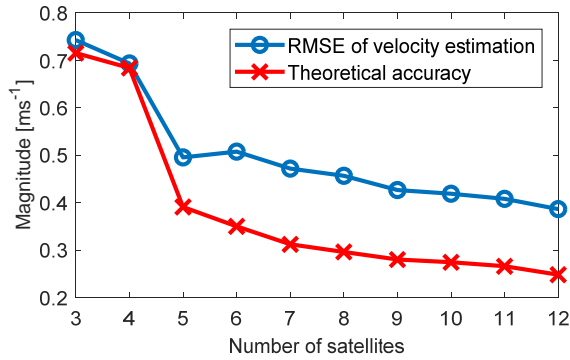Fig. 15. The vertical velocity component of Target B.

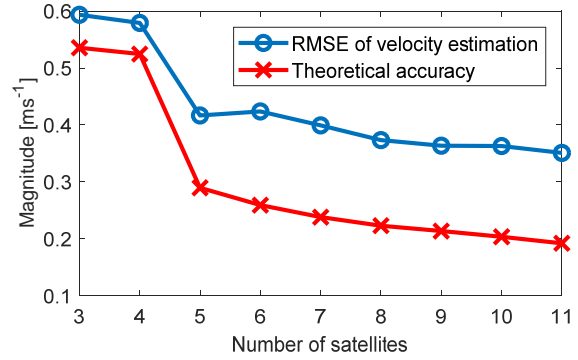Fig. 16. RMSE of velocity vector estimation result for Target A.

Fig. 17. RMSE of velocity vector estimation result for Target B.

different number of satellites are plotted in one figure and separated with different colors. Alternatively, we have also conducted the velocity estimation processing using AIS position as the input for different numbers of satellites as well, and the results by AIS are also provided in the same figure, i.e. Fig.10 for target A, shown as the dotted black curves. The results using the same number of satellites are put together, as shown in Fig.10, one is solid color curve, denoting the position by the target localization is used, while the other is the dotted black curve, denoting the AIS position is used. From fig.10, it is seen that to use which target position does not affect the velocity estimation results a lot. Likewise, Fig.11 provides the corresponding horizontal speeds for target B.

Since there are not big differences in the speed range between the values of different satellites, the curves are arranged from top to bottom, in the order of increasing numbers of satellites, with the dotted horizontal line in corresponding colors to give a same reference value. A scale bar of 1 ms^{-1} is given for estimating the dynamic range of each curve.

When it comes to the direction of the target velocity, it is described as the North-based azimuth, as the results for Target A shown in Fig.12 as an example. Note that our recorded AIS track is a jagged line, so the calculated velocity from AIS is after smoothing approaches, inevitably resulting in loss of accuracy, especially in terms of the direction, but this AIS reference is still given as the reference.

Since the velocity estimation is considered as a three-dimensional problem, Fig.14 and Fig.15 demonstrate the vertical speeds for target A and B respectively, indicating the ups and downs of the ferries. From the results, the vertical speed is basically around zero and within a range of 1ms^{-1}, a reasonable result for the ferry that are observed, and this range decreases with the increase of the number of satellites.

From the results of Fig.10-15, it can be seen that, as expected, a larger number of satellites can yield a smoother estimate of the velocity versus time, in terms of both magnitude and azimuth. The detected velocity direction varies smoothly versus time and agrees very well with the tendency of the AIS target track (see Fig.3). The small vibration of the azimuth is within one or two degrees when the number of satellites reaches 11 or 12.

For the magnitude estimation, once the number of satellites has reached around five, further increases in their number do not show any further significant improvement. As a further test,

in order to exclude the influence of errors in the estimate of the target position on the velocity estimates, we have also processed the velocity estimates for different numbers of satellites using the AIS data to provide the target position. These results are also plotted on same figures, using black chained dotted lines. The difference of these results and their corresponding colored results are very small. This confirms a prediction that the velocity estimation accuracy mainly depends on the Doppler frequency precision and the spatial diversity of the satellites distribution, rather than the target positioning accuracy. There is only one exception that the target position accuracy has more effect when the target is crossing the shortest distance line to the receiver in a nearly-orthogonal direction. In that case, the target motion yields near-zero Doppler to many satellites, so that not enough information is available for velocity estimation. One example of this can be found in the period from 90 s to 100 s in Fig.11. In the results of this section, the estimated velocity varies rapidly, and probably not correctly, whatever the combination of satellites used. This section corresponds to the top-left part of the sky-blue line (Target B – 'Bretagne') in Fig.3.

To get a numerical understanding of the precision improvement as the number of satellites increases, we calculated the root mean square error (RMSE) of the estimated target velocity from the reference velocity calculated by the AIS track, in cases of different numbers of satellites. Fig.16 and Fig.17 gives the RMSE calculation results for two targets, in comparison with the theoretically calculated variance of the velocity using the method described in Section II.D. It should be noted here that the AIS data are used only for the experimental error analysis, while the theoretical error is obtained by extracting the stochastic components from the experimental, radar data only. The entire process is composed of the following steps:

i. Obtain the experimental target velocity v_E using the method in Section II.C.
ii. Calculate the target velocity reference v_R given by the AIS ground truth.
iii. Calculate the experimental velocity error e_{E-v} by the RMSE of (v_E-v_R), which gives the results marked by 'o' in Fig.16 and 17.
iv. Calculate the theoretical Doppler error e_{R-fd} according to the SNR for each target by [CPI/sqrt(SNR)].
v. Obtain the theoretical target location error e_{R-l} using the

method in [13].

vi. Obtain the velocity error reference e_{R-v} using the method in section II.D and based on e_{R-fd} and e_{R-l}, which gives the results marked by 'x' in Fig.16 and 17.

We can observe a high degree coincidence of the measured RMSE with the theoretical results, which confirms the accuracy estimation method for the target velocity vector estimation. It should be noted that the reference Doppler derived from the AIS might not actually be same as the 'true' values, due to the limitations in the accuracy of the AIS data. This may be a significant contributor to the offset between the theoretical and observed accuracies seen in Fig 16 and Fig. 17. Furthermore, the theoretical accuracy calculation also assumes that the reference point on the ship used by the AIS data logger is at the 'centre of gravity' of its radar signature. The RMSE for both targets can be seen to monotonically decrease as the number of satellites increases.

It can be seen that the propagation of the Doppler errors through the process of estimating the velocity leads to an error which is approximately twice what would be theoretically be expected for large numbers of satellites. For small numbers of satellites, of course, the estimation behaves almost exactly as expected. We note in passing that the errors of a point target would be about an order of magnitude lower than for the extended target.

The velocity estimated accuracy for Target A and B with the maximum number of satellites are approximately 0.39 ms^{-1} and 0.35 ms^{-1} respectively. We can deduce the true values of the average velocities relatively accurately by dividing the total distance moved, as reported by the AIS, by the entire time. This gives the average velocities of the reference of 5.46 ms^{-1} and 5.41 ms^{-1} over the observation times of 110 s and 100 s respectively for two targets. Hence we can calculate that the accuracy is around 7%. The accuracy of the velocity estimation has also verified the accuracy of the bistatic Doppler measurements.

Therefore, the performance of the multistatic technique to be applied for target velocity estimation, as well as the accuracy estimation method, have been validated by the experimental results of practical maritime GNSS-based radar.

V. CONCLUSIONS

A method has been presented of estimating the target velocity from measurements made by a passive multistatic radar system, composed of multiple transmitters and one single receiver.

The expected accuracy of the estimation scheme has been calculated theoretically. The method for estimating velocity and its accuracy have been confirmed by measurement. The data show that the largest improvement in accuracy occurs by considering 6 satellites, however still as more satellites are included the increase in performance is notable albeit not as rapid.

For the experimental validation, we have used a multistatic GNSS-based radar system although the algorithms can also be applied directly to other multistatic illuminators, with other geometries.

A more complete system uses reflected signals from multiple GNSS constellations. The experiments were conducted using a multistatic acquisition geometry with maritime ferries as the targets of opportunity. The target reflections are successfully tracked from in total 12 satellites from the Galileo, Glonass and GPS constellations. Different numbers of satellites are used for the estimation of the target velocity. Comparing the results, the maximum number of 11 or 12 satellites can provide a relatively high velocity accuracy.

The relationship between the errors in the raw Doppler measurements for an extended target and the velocities estimates is very well understood for the combination of measurements for small numbers of satellites is well understood and is reasonably-well understood for the combination of measurements from a large number of satellites.

The velocity estimates obtained from the real extended targets are about an order of magnitude less accurate than would be expected from a point target.

In order to prove the concept, the measurements were made with relatively large targets and at short ranges to ensure that clear results could be obtained. One aspect for future research, therefore would be to explore the sensitivity available from this technique against smaller targets, including improvement of the detection capability, for example by means of further multistatic data fusion techniques.

REFERENCES

[1] H. Griffiths, C. Baker, "Passive Bistatic Radar," Principles of Modern Radar: Volume 3: Radar Applications, *IET Digital Library*, 2013:499-541.

[2] F. Colone, D. W. O'hagan, P. Lombardo, C. J. Baker, "A multistage processing algorithm for disturbance removal and target detection in passive bistatic radar," *IEEE Trans. Aerosp. Electron. Syst.*, vol. 45, no. 2, pp. 698-722,Apr. 2009.

[3] M. Conti, F. Berizzi, M. Martorella, E.D. Mese, D. Petri, and A. Capria, "High range resolution multichannel DVB-T passive radar," *IEEE Aerosp. Electron. Syst. Mag.*, vol. 27, pp. 37-42, Oct. 2012.

[4] D. Langellotti, F.Colone, P.Lombardo, E.Tilli, M.Sedehi, A.Farina, "Over the horizon maritime surveillance capability of DVB-T based passive radar," in *IEEE Microwave Conference (EuMC), 2014 44th European*, Rome, Italy, Oct. 2014.

[5] M. Daun, U. Nickel, W. Koch, "Tracking in multistatic passive radar systems using DAB/DVB-T illumination." *Signal Processing*, vol. 92, no. 6, pp. 1365-1386, 2012.

[6] H. Sun, D. K. Tan, Y. Lu,"Aircraft target measurements using a GSM-based passive radar," in *IEEE Radar Conference*, Rome, Italy, 2008, pp. 1-6.

[7] R. Zemmari, M. Daun, M. Feldmann, U. Nickel, "Maritime surveillance with GSM passive radar: Detection and tracking of small agile targets," In *International Radar Symposium (IRS),* Dresden, Germany, Jun. 2013.

[8] F. Colone, P. Falcone, C. Bongioanni, and P. Lombardo, "WiFi-based passive bistatic radar: data processing schemes and experimental results," *IEEE Trans. Aerosp. Electron. Syst.*, vol. 48, pp. 1061-1079, 2012.

[9] H. Thomas, T. Webster and E. L. Mokole, "Passive multistatic radar experiment using WiMAX signals of opportunity. Part 1: Signal processing," *IET Radar, Sonar & Navigation*, vol. 10, no. 2, pp. 238-247, Jan. 2015.

[10] T. Webster, H. Thomas and E. L. Mokole, "Passive multistatic radar experiment using WiMAX signals of opportunity. Part 2: Multistatic velocity backprojection," *IET Radar, Sonar & Navigation*, vol. 10, no. 2, pp. 248-255, Jan. 2015.

[11] M. Antoniou and M. Cherniakov, "GNSS-based bistatic SAR: A signal processing view," *EURASIP Journal on Advances in Signal Processing*, no.1, pp. 1-16, Mar. 2013.

[12] F. Liu, M. Antoniou, Z. Zeng, and M. Cherniakov, "Coherent change detection using passive GNSS-based BSAR: experimental proof of

concept," *IEEE Trans. Geosci. Remote Sens.*, vol. 51, no. 8, pp. 4544-4555, Aug. 2013.

[13] M. Malanowski and K. Kulpa, "Two methods for target localization in multistatic passive radar," *IEEE Trans. Aerosp. Electron. Syst.*, vol. 48, no. 1, pp. 572-580, Jan. 2012.

[14] P. Falcone, F. Colone, A. Macera, and P. Lombardo, 'Twodimensional loeation of moving target within local areas using WiFi-based multistatic passive radar," lET Radar Sonar Navig., vol. 8, no. 2, pp. 123-131,2014.

[15] B. K. Chalise, Y. D. Zhang, M. G. Amin, and B. Himed, "Target localization in a multistatic passive radar system through eonvex optimization," Signal Process., vol. 102, pp. 207-215, Sep.2014.

[16] B. K. Habtemariam, R. Tharmarasa, T. Kirubarajan, D. Grimmett, C. Wakayama, "Multiple Detection Probabilistic Data Association filter for multistatic target tracking," in *Proceedings of the International Conference on Information Fusion*. 2011.

[17] B. Sobhani, E. Paolini, A. Giorgetti, M. Mazzotti, M. Chiani, "Target tracking for uwb multistatic radar sensor networks," *IEEE Journal of Selected Topics in Signal Processing*, vol. 8, no. 1, pp. 125-136, Feb. 2014.

[18] H. Yang and J. Chun, "An improved algebraic solution for moving target localization in noncoherent MIMO radar systems," IEEE Trans. Signal Process., vol. 64, no. 1, pp. 258–270, Jan. 1, 2016.

[19] A. Noroozi and M. A. Sebt, "Target localization in multistatic passive radar using SVD approach for eliminating the nuisance parameters," IEEE Trans. Aerosp. Electron. Syst., vol. 53, no. 4, pp. 1660–1671, Aug. 2017.

[20] H. Ma, M. Antoniou, D. Pastina, F. Santi, F. Pieralice, M. Bucciarelli, Mikhail Cherniakov, "Maritime Moving Target Indication Using Passive GNSS-Based Bistatic Radar", *IEEE Transactions on Aerospace and Electronic Systems*, vol. 54, no. 1, pp. 115 - 130, Feb. 2018.

[21] H. Ma, M. Antoniou, A. G. Stove, J. Winkel, M. Cherniakov, "Maritime Moving Target Localization Using Passive GNSS-based Multi-static Radar", *IEEE Trans. Geosci. Remote Sens.*, accepted for publication.

[22] I. Cohen, N. Levanon, "Contribution of Auxiliary Coherent Radar Receiver to Target's Velocity Estimation", *IET Radar Sonar Navigation*, vol. 12, no. 3, pp. 287-293, Mar. 2018.

[23] C. Shi, F. Wang, J. Zhou, "Cramér–Rao bound analysis for joint target location and velocity estimation in frequency modulation based passive radar networks", *IET Signal Processing*, vol. 10, no. 7, pp. 780-790, Sep. 2016.

[24] Q. He, J. Hu, R. S. Blum, Y. Wu, "Generalized Cramér–Rao Bound for Joint Estimation of Target Position and Velocity for Active and Passive Radar Networks", *IEEE Trans. Signal Process.*, vol. 64, no. 8, pp. 2078-2089, Apr. 2016.

[25] Q. Wu, Y. D. Zhang, M. G. Amin, B. Himed, "Space–time adaptive processing and motion parameter estimation in multistatic passive radar using sparse bayesian learning", *IEEE Trans. Geosci. Remote Sens.*, vol. 54, no. 2, pp. 944-957, Feb. 2016.

[26] M. Radmard, S. Karbasi, and M. Nayebi, "Data fusion in MIMO DVB-T-based passive coherent location," *IEEE Trans. Aerosp. Electron. Syst.*, vol. 49, no. 3, pp. 1725-1737, Jul. 2013.

[27] A. Noroozi and A. S. Mohammad, "Target localization from bistatic range measurements in multi-transmitter multi-receiver passive radar," *IEEE Signal Process. Lett.*, vol. 22, no. 12, pp. 2445-2449, Oct. 2015.

[28] M. Edrich, A. Schroeder and F. Meyer, "Design and performance evaluation of a mature FM/DAB/DVB-T multi-illuminator passive radar system," *IET Radar, Sonar & Navigation*, vol. 8, no. 2, pp. 114-122, Feb. 2014.

[29] A. H. Oveis and M. A. Sebt, "Coherent method for ground-moving target indication and velocity estimation using Hough transform", *IET Radar, Sonar & Navigation*, vol. 11, no. 4, pp. 646-655, Apr. 2017.

[30] D. Pastina, F. Santi, F. Pieralice, M. Bucciarelli, H. Ma, D. Tzagkas, M. Antoniou, M. Cherniakov, "Maritime moving target long time integration for GNSS-based passive bistatic radar," *IEEE Trans. Aerosp. Electron. Syst.*, vol. PP, no. 99, pp. 1-22, May 2018.